Comparative analysis of internal energy excitation and dissociation of nitrogen predicted by independently developed *ab initio* potential energy surfaces

Maninder S. Grover● and Paolo Valentini●

University of Dayton Research Institute, 1700 South Patterson Boulevard, Dayton, Ohio 45469, USA

Thomas E. Schwartzentruber

Department of Aerospace Engineering and Mechanics,
University of Minnesota, Minneapolis, Minnesota 55455, USA

Richard L. Jaffe

NASA Ames Research Center, Moffett Field, California 94035, USA

Nicholas J. Bisek● and Ashley M. Verhoff●

Air Force Research Laboratory, Wright-Patterson Air Force Base, Ohio 45433, USA

In this article we present a comparative atomic level study analyzing the vibrational excitation and dissociation of molecular nitrogen due to $N_2(^1\Sigma_g{}^+) + N(^4S_u)$ and $N_2(^1\Sigma_g{}^+) + N_2(^1\Sigma_g{}^+)$ interactions governed by independently developed potential energy surfaces at the University of Minnesota and NASA Ames Research Center. Vibrational excitation was studied for $N_2 + N_2$ interactions from $T = 10\,000$ to $25\,000$ K and for $N_2 + N$ from $T = 5000$ to $30\,000$ K. Nonequilibrium dissociation is studied from $T = 10\,000$ to $30\,000$ K under the quasi-steady-state condition for $N_2 + N_2$ and $N_2 + N$ interactions. Finally, an inviscid Mach 20 dissociating nitrogen flow over a cylinder with a Knudsen number of 0.015 is carried out to study the impact of molecular interactions predicted by independently developed potential energy surfaces on a canonical hypersonic flow.

I. INTRODUCTION

Strong shocks generated at the bow of reentry vehicles cause the gas temperature to rise to thousands of kelvin. The postshock heated gas experiences excitation of internal energy modes and chemical reactions. However, given the relatively low air density at high altitudes and the high speed of the flow, the rate of internal energy excitation and chemical reactions often competes with local characteristic flow times. This causes the gas enveloping the vehicle to be in thermal and chemical nonequilibrium [1]. The rate laws in computational fluid dynamics (CFD) solvers used to capture these phenomena are based on experimental data from the 1960s and 1970s [2–4]. These rates often vary by orders of magnitude between different experimental data sets, as seen in Refs. [5–8], and need to be extrapolated to temperatures encountered in reentry flight. The base variance in the rate laws and their nonlinear nature introduce significant uncertainty in CFD calculations.

In recent years there have been efforts to complement the experimental databases of thermochemical properties with high-fidelity data from computational chemistry. In this approach, an interaction potential is first generated for the particle interaction of interest. This is done by solving the electronic Schrödinger equation [9–15] to generate single-point energies for thousands

of geometries of the interaction of interest and then sophisticated fitting techniques, typically leveraging polynomial forms [9–15] or neural networks [16,17], are used to generate a mathematically smooth potential energy surface (PES). Potential energy surfaces derived in this manner are often termed first-principle or *ab initio* PESs. These PESs are then leveraged to calculate scattering trajectories [18,19], aggregates of which are used to determine the thermochemical and kinetic properties.

A common method for using these scattering trajectories is the state-to-state (STS) method [20–23]. In this approach, a large number of trajectory calculations are performed at predetermined conditions. These trajectories are then used to derive molecular internal energy state transition rates and state specific chemical reaction rates. A database of state transition rates is then incorporated into a flow solver that evaluates the master equation [20] and tracks each internal state as a pseudospecies in the flow [23–27]. These solvers are used to conduct zero-dimensional (0D) reactor simulations [27–29] to determine thermochemical properties. Even though the STS method is a powerful approach, it can become intractable for molecule-molecule interactions. For example when all quantized rovibrational states are taken into account, there are of the order of 10^{15} possible state transitions for $N_2 + N_2$ interactions. To make STS simulations feasible for such systems, energy states are binned together [26,27,30–32]. However, it has been shown that binning of internal states leads to a loss of information about relaxation between internal states, which can cause variations in macroscopic thermochemical properties based on binning strategy [33]. Since the scattering trajectory calculations done using *ab initio* PESs are expensive and have to be completed *a priori* to STS simulations, this often translates to these simulations being run on sparsely populated data sets that may not have adequate resolution for every relevant state transition in a flow simulation. Thus, STS simulations have to interpolate between state transition rates which follow nonlinear trends in the temperature range of interest. Furthermore, as the construction of the state transition database requires significant investment in running scattering trajectories, STS methods are more rigid to adapt to newer PESs or to explore state transitions given by different PESs.

In this work we use the direct molecular simulation (DMS) [34] approach. Unlike the STS method [20] described above, DMS implements the scattering trajectory calculation within a time-accurate flow-field simulation. In this way the DMS method bypasses the need for binning energy states and is able to capture all statistically significant state transitions in a given simulation. Therefore, DMS simulations have no *a priori* assumptions and use the relevant PES(s) as the only modeling input for the calculation. The ability to run scattering collisions on the fly also makes DMS an ideal tool to substitute different PESs for the same system to conduct a comparative study. In the past the DMS method has been used to calculate thermochemical properties in 0D reactors [35–39] and 1D shock calculations [40] and recently has been expanded to study 2D hypersonic flow [41–43] and transport properties [44]. In this study we consider independently developed PESs at the University of Minnesota [9,10] and NASA Ames Research Center [11,12] designed to capture high-energy $N_2 + N_2$ and $N_2 + N$ collisions using different computational chemistry techniques. The objective of this work is to compare thermochemical properties predicted by these PESs. This is achieved by (i) conducting 0D isothermal heat bath studies to calculate and compare characteristic vibrational excitation times, (ii) comparing nonequilibrium dissociation rate coefficients using a 0D reactor under quasi-steady-state conditions, (iii) comparing molecular level details such as the energy distribution functions predicted under nonequilibrium conditions, and (iv) comparing flow-field features due to a Mach 20 dissociating nitrogen flow over a 2D cylinder.

II. DIRECT MOLECULAR SIMULATION

A. Method overview

A detailed description of the DMS method can be found in Ref. [34]; this section provides only a brief overview for clarity. The DMS method is a high-fidelity variant of the direct simulation

Monte Carlo (DSMC) method of Bird [45]. Similar to DSMC, the DMS is a particle method that predicts flow characteristics by aggregating particle properties in a simulation cell. The simulation time steps are of the order of the mean collision time τ_c, the simulation cell sizes are of the order of the local mean free path λ_c, and the ratio of the actual particles to the simulated particles in the control volume is called the particle weight W_p. Every time step a representative number of particles in the simulation domain are selected to undergo collisions to approximate the mean collision rate of the gas. However, where the standard DSMC approach uses stochastic collision models, the DMS method carries out scattering trajectory calculations using the appropriate PES [19,34] to determine the collision outcome.

When a particle pair is selected for trajectory integration, the phase-space coordinates of all atoms of the colliding particles are integrated using a velocity Verlet scheme [46]. The time step for trajectory integration is set to $\Delta t_{\text{traj}} = 0.05$ fs. The trajectory is integrated until the minimum separation between the atoms not bounded to the same molecule is greater than the minimum cutoff distance $D_0 = 15$ Å. During a trajectory, for certain atomic configurations, the atoms may go over local free-energy maxima in the PES. This may lead to the formation of new bonds and breaking of others. Hence, the DMS method automatically accounts for all collision outcomes available in the PES. After the trajectory integration is completed, each molecule is analyzed to establish if it is bound, quasibound, or dissociated. Then as a postprocessing step the internal energy of the molecule is calculated using the position and velocity of the bound atoms. Currently, the DMS method does not allow for recombination of atomic species back to molecules as research is actively being conducted in the proper treatment of three-body collisions and recombination for scattering trajectories [47,48].

The 0D reactor simulations discussed in Sec. III are obtained using an in-house DMS code developed at the University of Minnesota and the 2D simulations shown in Sec. IV are obtained by incorporating DMS routines in the stochastic parallel rarefied-gas time-accurate analyzer DSMC code developed at Sandia National Laboratories [49]. Details of this implementation are discussed in Refs. [41,42].

B. Potential energy surfaces

This section provides a high-level overview of the PESs used in this study. A PES is a fit to the potential energy of various atomic arrangements of the interacting system. The gradients of the PES are used to perform the molecular trajectory calculation as discussed in Sec. II A and the PESs serve as the only modeling input to the DMS method. Early attempts at defining PESs were based on a combination of theoretical calculations and empirical data from experiments [50–55]. These PESs are often represented with simple analytical functions. However, due to the simplicity of the fitting functions and use of inadequate data to resolve atomic interactions [56], such PESs are less accurate for modeling molecular interactions involving high collision energy. In recent years, PESs tailored to capture high-energy interactions have been produced [9–15]. These potential energy surfaces are derived from extensive quantum-mechanical calculations, where the electronic Schrödinger equation is solved to give the potential energy of the interacting nuclei. These PESs derived from first principles are called *ab initio* PESs. In this work we use *ab initio* PESs developed at the University of Minnesota and NASA Ames Research Center.

The group at NASA Ames Research Center developed separate PESs for $N_2 + N_2$ interactions (NASA N_4 PES) and $N_2 + N$ interactions (NASA N_3 PES). The details of the NASA PESs can be found in Refs. [11,12,56]. Broadly, both NASA PESs use an augmented correlation consistent polarized valence triple zeta (aug-cc-pVTZ) [57,58] basis set. The aug-cc-pVTZ basis set contains five s orbitals, four p orbitals, three d orbitals, and two f orbitals for each atom. The NASA PESs utilize two different methods to compute electron correlation. The coupled-cluster method, the coupled cluster with single and double and perturbative triple excitations (CCSD(T)) [59], was used for geometries where two distinct nitrogen molecules exist. For other geometries the multireference configuration interaction (MRCI) [60] method is used with complete active space self-consistent

TABLE I. Properties of diatomic nitrogen from the potential energy surfaces developed at the University of Minnesota [9,10] and NASA Ames Research Center [11,12].

Quantity	UMN PES	NASA PES
dissociation energy at $j = 0$ (eV)	9.91	9.89
number of vibrational levels for $j = 0$	55	61
number of rotational levels for $v = 0$	279	279
number of rovibrational levels	9198	9390
number of bound rovibrational levels	7122	7421
number of quasibound rovibrational levels	2076	1969

field (CASSCF) [61] molecular orbitals. The NASA N_4 PES has 4146 single energy points, with 3821 points obtained from CCSD(T) and 325 points from CASSCF MRCI. The NASA N_3 PES has 3885 single energy points calculated using CCSD(T). Additionally, both NASA PESs use the diatomic potential energy function proposed by Le Roy *et al.* [62] to describe the N_2 diatom.

The PES developed at the University of Minnesota (UMN PES) [9,10] uses a minimally augmented correlation consistent polarized valence triple zeta (maug-cc-pVTZ) basis set [63]. This maug-cc-pVTZ formulation is similar to the aug-cc-pVTZ formulation discussed above but ignores some d orbitals and f orbitals from the augmentation set [63]. The PES also uses the CASSCF [61] used to obtain molecular orbitals. The UMN group uses a complete active space second-order perturbation theory (CASPT2) method [64–66] to obtain all single-point energies. The UMN PES has a total of 16 547 single-point energies, out of which 1017 were calculated for the $N_2 + N$ system. As such, this PES is able to resolve both $N_2 + N_2$ and $N_2 + N$ interactions [36]. The properties of diatomic N_2 as given by these PESs are shown in Table I. The differences in the numbers of bound and quasibound levels between UMN and NASA PESs are mainly due to small differences in the long-range nature of the diatomic potentials.

C. Treatment of internal energy

The DMS method operates on atomic positions and velocities. For atoms bound in a molecule, atomic positions and velocities may be postprocessed to obtained the rovibrational internal energy of the molecule [34]. Therefore, DMS calculations do not assume any *a priori* decoupling between rotational vibrational modes. To divide the internal energy into rotational and vibrational modes, the vibrational prioritization framework as discussed in Ref. [67] is used. In this framework, the internal rovibrational energy $\varepsilon_{\text{int}}(v, j)$ is used to calculate the vibrational (v) and rotational (j) levels of the molecule. Then the molecule is assigned the vibrational energy of level v corresponding to rotational level $j = 0$,

$$\varepsilon_{\text{vib}}(v) = \varepsilon_{\text{int}}(v, 0). \tag{1}$$

The remaining internal energy is assigned to the rotational mode

$$\varepsilon_{\text{rot}}(j) = \varepsilon_{\text{int}}(v, j) - \varepsilon_{\text{int}}(v, 0). \tag{2}$$

To characterize macroscopic evolution of the rotational mode in this article, rotational temperature is defined as the average rotational energy normalized by Boltzmann's constant

$$T_r = \frac{\langle \varepsilon_{\text{rot}} \rangle}{k_B}. \tag{3}$$

Similarly, in this article the average energy in the vibrational mode is used to define vibrational temperature as

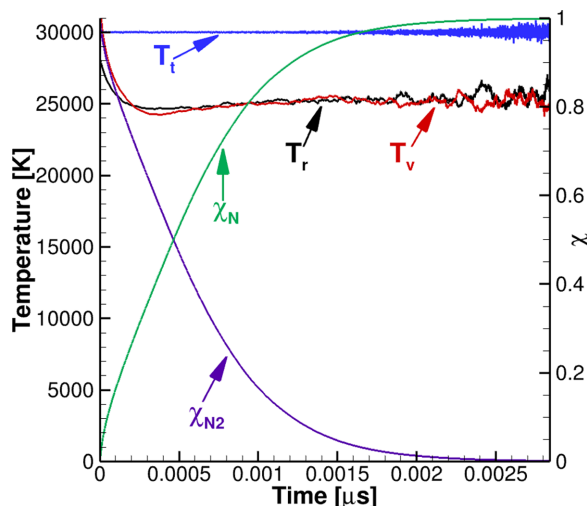$$T_v = \frac{\langle \varepsilon_{\text{vib}} \rangle}{k_B}. \tag{4}$$

FIG. 1. Example of isothermal relaxation in a box and formation of the QSS for the full nitrogen system (both $N_2 + N_2$ and $N_2 + N$ interactions allowed) using the NASA Ames PESs [11,12].

III. THERMOCHEMICAL PROPERTIES

A. Zero-dimensional isothermal reactor

Isothermal 0D reactor simulations are used to study and compare characteristic vibrational excitation (Sec. III B) and nonequilibrium dissociation (Sec. III B) due to $N_2 + N_2$ (N_4) and $N_2 + N$ (N_3) interactions separately. Then 0D isothermal reactors are used to assess the behavior of a system characterized by both N_4 and N_3 interactions. For the isothermal simulations presented in this section, the desired temperature is maintained by sampling particle center-of-mass velocities from a corresponding Maxwell-Boltzmann distribution and the density is set to $\rho = 1.28 \ \text{kg/m}^3$.

Figure 1 shows the time-dependent composition and temperature profiles of an isothermal 0D DMS calculation at $T = 30\,000$ K. In this example, the gas is initialized such that at $t = 0 \ \mu$s the translational (blue), rotational (black), and vibrational (red) temperatures are in equilibrium $T_t = T_r = T_v = 30\,000$ K. As the system evolves dissociation results in the decrease in the mass fraction of molecular nitrogen (purple) and an increase in mass fraction of atomic nitrogen (green). Due to dissociation, the population of molecules with higher rotational and vibrational energies is depleted. As seen in Fig. 1, this causes the average rotational and vibrational energies to decrease from the equilibrium value at $t > 0$. As the inelastic collisions and exchange reactions [36,68] repopulate the higher-energy states, a new balance is achieved between repopulation and depletion of higher internal energy levels. This balanced state is termed the quasi-steady-state (QSS) and is characterized by time-invariant internal energy distributions and stabilization of average internal energies. It can be seen in Fig. 1 that this system reaches QSS around $t = 0.001 \ \mu$s.

Figure 2(a) shows the Boltzmann and QSS vibrational energy distribution at $T = 30\,000$ K. It can be seen that the QSS vibrational energy distribution is non-Boltzmann and has a depleted population at the higher vibrational energy levels when compared to the corresponding Boltzmann distribution. Similarly, Fig. 2(b) shows the Boltzmann and QSS rotational energy distribution. The QSS rotational distribution is non-Boltzmann and has depleted populations at the higher rotational levels. The QSS is a consequence of repopulation of high-energy states by inelastic collisions and depletion due to collisions that result in dissociation, so the QSS depends only on the local collision rate. In other words, the QSS is uniquely defined for a given temperature and density of the gas and is independent of the initial internal energy state of the isothermal reactor. This conclusion is illustrated by Fig. 2(c). In the figure, the translational temperature (blue) is held constant at $T_t = 30\,000$ K and
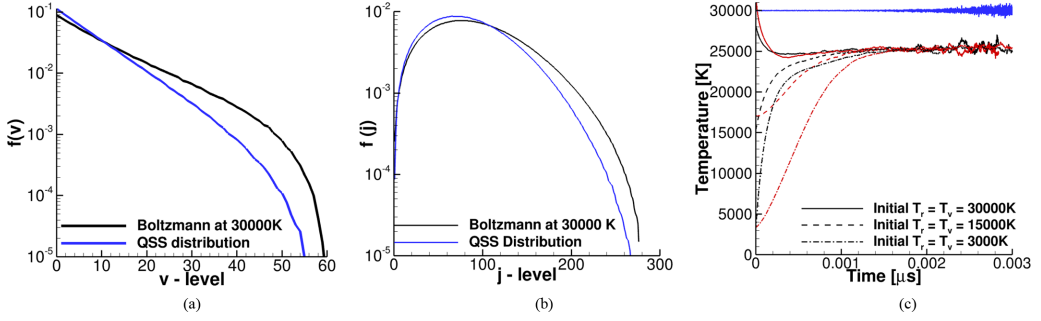
FIG. 2. Characteristics of the QSS at $T = 30\,000$ K, at (a) Vibrational Energy Distribution in QSS, (b) Rotational Energy Distribution in QSS and (c) QSS for various initial internal energy states of the gas.

then the rotational (black) and vibrational (red) temperatures are initialized at $T_r = T_v = 30\,000$, $15\,000$, and 3000 K. It can be seen that, regardless of the initial internal temperature that is assigned to the gas, the systems stabilizes to the same QSS.

B. Characteristic vibrational excitation time

Characteristic vibrational excitation times are derived by conducting 0D isothermal relaxation calculations as described above. The temporal profiles of the average vibrational energy are fit to the solution of a first-order ordinary differential equation

$$\frac{d\langle \varepsilon_{\text{vib}}(t)\rangle}{dt} = \frac{\langle \varepsilon_{\text{vib}}^*\rangle - \langle \varepsilon_{\text{vib}}(t)\rangle}{\tau_{\text{vib}}} \tag{5}$$

to determine τ_{vib}. Here $\langle \varepsilon_{\text{vib}}(t)\rangle$ is the instantaneous value of the average vibrational energy and $\langle \varepsilon_{\text{vib}}^*\rangle$ is the average vibrational energy under equilibrium conditions.

To calculate the characteristic vibrational excitation time due to $N_2 + N_2$ interactions ($\tau_{\text{vib}}^{N_2+N_2}$), $N_2 + N$ interactions are excluded in the heat bath calculations. The results of these calculations are shown in Fig. 3. The DMS calculations using the NASA N_3 PES (blue squares with solid line) and
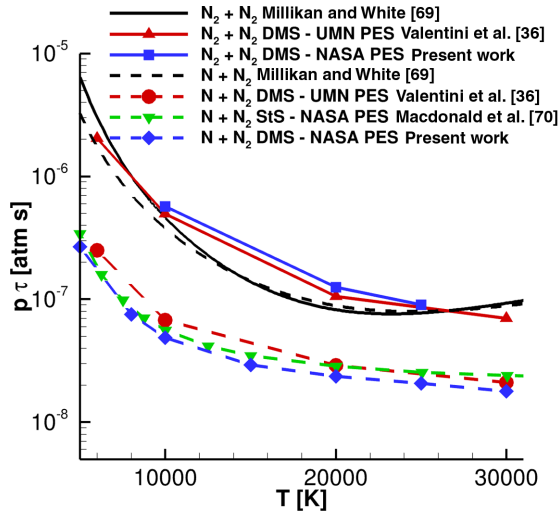

FIG. 3. Characteristic vibrational excitation times for $N_2 + N_2$ and $N_2 + N$ interactions.

the UMN PES (red triangles with solid line) produce qualitatively similar results, with the maximum variation between $\tau_{\text{vib}}^{N_2+N_2}$ predicted by the two PESs being about approximately 16% at 10 000 K. The difference in the predicted $\tau_{\text{vib}}^{N_2+N_2}$ decreases with an increase in temperature. Furthermore, it is observed that the DMS results for $\tau_{\text{vib}}^{N_2+N_2}$ match closely with the Millikan-White fit [2,69] (black solid line) for the characteristic vibrational excitation time. However, while the high-temperature correction of Park [2] causes the characteristic excitation time to increase past 20 000 K, the DMS calculations show that the characteristic excitation time keeps decreasing.

To calculate characteristic vibrational excitation time due to $N_2 + N$ interactions ($\tau_{\text{vib}}^{N_2+N}$), 0D isothermal excitation calculations are carried out for a mixture of N_2 and N where the partial density of molecular nitrogen is initialized at $\rho_{N_2}/\rho = 0.01$. The DMS calculations using the NASA N_3 PES (blue diamonds with dashed line) and the UMN PES (red circles with dashed line) are seen to produce qualitatively similar results, with the maximum variation between the predicted $\tau_{\text{vib}}^{N_2+N}$ from the two PESs approximately 28% at 10 000 K, with the difference in $\tau_{\text{vib}}^{N_2+N}$ decreasing with an increase in temperature. When comparing the STS calculations of Macdonald *et al.* [70] (green inverted triangles with dashed line) we see excellent agreement for the predicted $\tau_{\text{vib}}^{N_2+N}$ at lower temperatures. The difference between the predicted $\tau_{\text{vib}}^{N_2+N}$ values increases with an increase in temperature, resulting in a maximum difference of approximately 33% at the maximum calculated temperature of 30 000 K. Note that Macdonald *et al.* [70] used the same NASA N_3 PES as this work; therefore, the difference in the results is due to the numerical approach. Finally, when compared to the Millikan-White fit [69], it can be seen that all computational chemistry results are approximately an order of magnitude lower. This faster excitation due to $N_2 + N$ interactions has been attributed to exchange reactions which have been shown to be more efficient in redistributing vibrational energy [36,68].

C. Nonequilibrium dissociation

In this section we discuss dissociation under QSS conditions. As discussed above, the QSS represents a balance between depletion and repopulation of high-energy levels and therefore provides a metric to compare the two kinds of molecular interactions on the PESs concurrently. A comparative analysis of dissociation under QSS purely due to $N_2 + N_2$ interactions given by the NASA and UMN PESs has been discussed in Ref. [56]. In this work we extend that analysis to $N_2 + N$ interactions and to the combined system where $N_2 + N$ and $N_2 + N_2$ interactions can occur simultaneously.

1. $N_2 + N$ *interactions*

In this section we discuss dissociation due to $N_2 + N$ collisions. As described in the preceding section (Sec. III B), in order to isolate the effects of atom-molecule collisions in DMS, isothermal 0D calculations were conducted for a mixture of nitrogen atoms and molecules where the partial density of molecular nitrogen is reduced to $\rho_{N_2}/\rho = 0.01$. The heat bath is then simulated until the system is in QSS. Once the system is in QSS the dissociation rate coefficient is calculated by fitting the temporal composition profile to the equation

$$\frac{d[N_2]}{dt} = -k_d^{N_2+N_2}[N_2]^2 - k_d^{N+N_2}[N][N_2]. \tag{6}$$

Since $[N_2] \ll [N]$ the first term in Eq. (6) is ignored and we assume that [N] does not change in time because, at $t = 0$, $[N] \gg [N_2]$. Therefore, $[N](t) \sim [N](t = 0) = [N]_0$. This reduces Eq. (6) to a pseudo-first-order rate law given by

$$\frac{d[N_2]}{dt} = -[N]_0 k_d^{N+N_2}[N_2]. \tag{7}$$

Figure 4(a) shows the QSS dissociation rate coefficients obtained from the above analysis. As seen, the dissociation rate coefficient in QSS, purely due to $N_2 + N$ interactions ($k_{d|\text{QSS}}^{N_2+N}$) predicted

(a) Dissociation rate coefficients in QSS given by DMS.a

(b) Comparison of DMS based dissociation rate coefficients and experimental and equilibrium data.
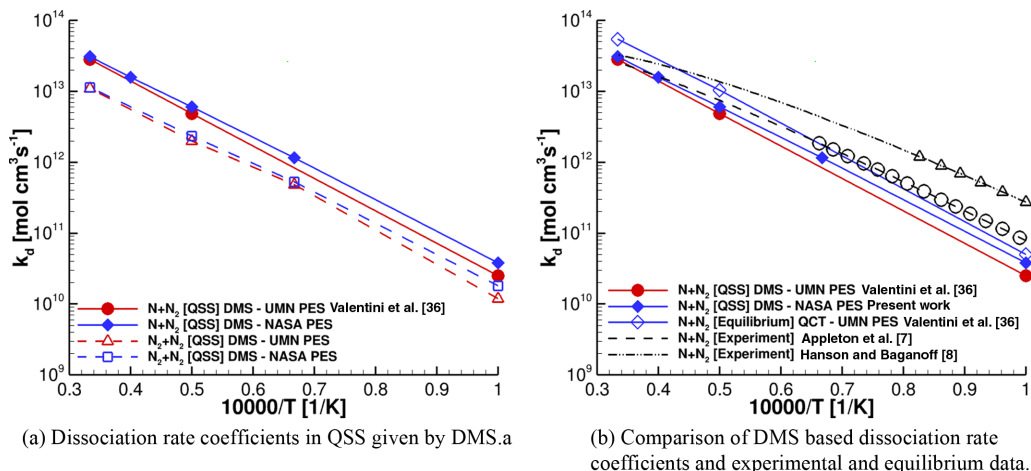
FIG. 4. (a) Dissociation rate coefficients in QSS given by DMS and (b) comparison of DMS-based dissociation rate coefficients and experimental and equilibrium data.

by the NASA PES (blue diamonds with solid line), is nearly 50% higher than $k_{d|QSS}^{N_2+N}$ predicted by the UMN PES (red circles with solid line) at $T = 10\,000$ K. However, this difference decreases with increasing temperature such that the difference is only 10% at $T = 30\,000$ K. Additionally, we provide a comparison of dissociation rate coefficients in QSS for systems where only $N_2 + N_2$ interactions were allowed. These data were first published in Ref. [56] and since then more statistics have been collected for the QSS dissociation rate coefficient at $10\,000$ K and an additional point of comparison has been added at $15\,000$ K. The QSS dissociation rate coefficient for $N_2 + N_2$ interactions ($k_{d|QSS}^{N_2+N_2}$) is 50% higher at $10\,000$ K for the simulation using the NASA PES (blue squares with dashed lines) when compared to the simulation using the UMN PES (red triangles with dashed line). The difference in predicted $k_{d|QSS}^{N_2+N_2}$ decreases with an increase in temperature and at $30\,000$ K the nonequilibrium dissociation rate coefficient differs by 4%.

Figure 4(a) also shows that the QSS dissociation rate for $N_2 + N$ interactions is higher than that for $N_2 + N_2$ interactions. This can be explained by Fig. 5, which shows the vibrational distribution function in QSS. It can be seen at $30\,000$ K [Fig. 5(a)], $20\,000$ K [Fig. 5(b)], and marginally at $10\,000$ K [Fig. 5(c)] that the QSS vibrational energy distribution is less depleted for the simulations that include $N_2 + N$ dynamics. This higher population of vibrationally excited molecules is attributed to faster vibrational relaxation due to $N_2 + N$ interactions as shown in

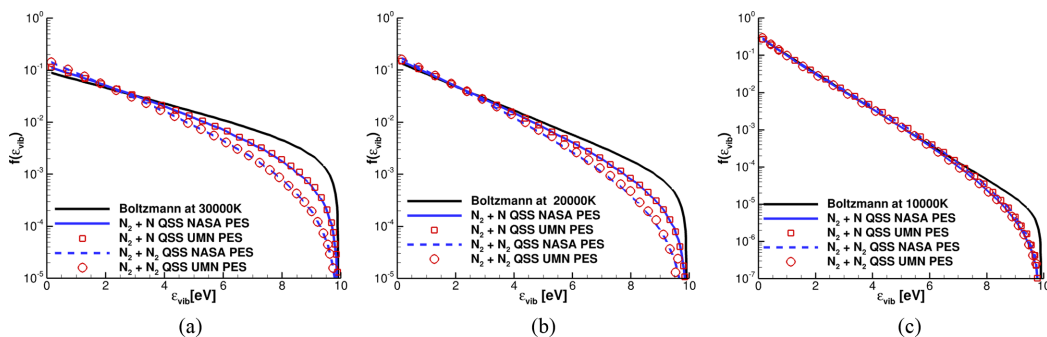FIG. 5. QSS vibrational distribution functions for 0D systems where only $N_2 + N$ or only $N_2 + N_2$ interactions are allowed, at (a) $30\,000$ K, (b) $20\,000$ K, and (c) $10\,000$ K.
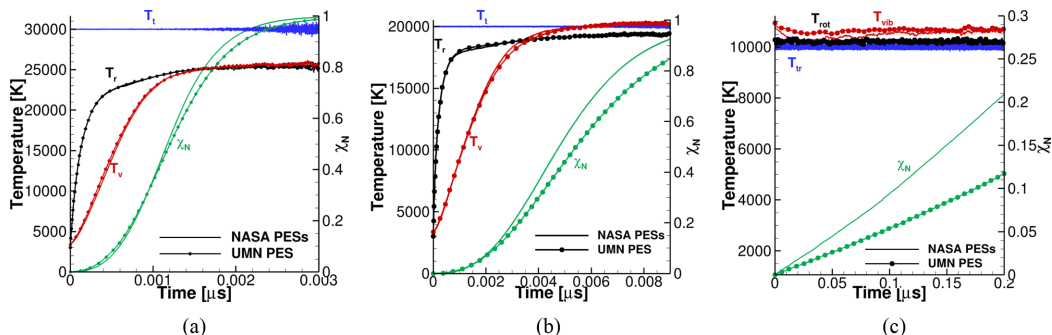
FIG. 6. Composition and temperature history comparison of simulations including both $N_2 + N$ and $N_2 + N_2$ interactions using the NASA PESs and the UMN PES, at (a) $T_t = 30\,000$ K, (b) $T_t = 20\,000$ K, and (c) $T_t = 10\,000$ K.

Sec. III B. Additionally, it can be seen that the vibrational energy distributions in QSS of simulations using the NASA PESs and the UMN PES agree well.

Figure 4(b) compares QSS dissociation rate coefficients with dissociation rate coefficients for $N_2 + N$ in equilibrium [36]. It can be seen that the dissociation rate coefficients in equilibrium are higher than the QSS rate coefficients, which can be attributed to the QSS energy distributions being depleted at higher-energy levels, as seen in Fig. 5. Additionally, Fig. 4(b) shows experimental data of Appleton *et al.* [7] and Hanson and Baganoff [8]. The symbols representing the experimental data show the temperature range for which the experiments were conducted. It can be seen that the variation between the experimental dissociation rate coefficients is larger than the difference in rate coefficients predicted from computational chemistry by the two PESs. Furthermore, as seen in Fig. 5, the vibrational energy distribution predicted by the two PESs in QSS is almost identical. This shows that at the atomistic level the two PESs predict similar rates of depletion and repopulation of the high-energy tail of the vibrational energy distribution.

2. $N_2 + N_2$ *and* $N_2 + N$ *interactions*

While the above sections have individually established the characteristics of $N_2 + N$ and $N_2 + N_2$ interactions, in this section we study the behavior of isothermal heat baths that allow for both interactions to occur concurrently. Figure 6 show the time evolution of temperature and composition in 0D heat baths at 30 000 K [Fig. 6(a)], 20 000 K [Fig. 6(b)], and 10 000 K [Fig. 6(c)]. The plots show the translational temperature (blue), rotational temperature (black), vibrational temperature (red), and mass fraction of atomic nitrogen (green). All three cases are initialized with pure molecular nitrogen in the reactor at $t = 0$ μs. The heat baths at 30 000 and 20 000 K show excitation of internal temperatures from 3000 K to a QSS state, whereas the heat bath at 10 000 K shows relaxation to QSS from an equilibrium state at $T = 10\,000$ K. These simulations show that the particle interactions predicted by the NASA PESs and UMN PES show a similar excitation rate for internal temperatures; however, the simulations using the NASA PESs allow for faster dissociation of molecular nitrogen.

Figure 7 shows the vibrational distribution function during the QSS for the simulations shown in Fig. 6. It can be seen that the two PESs predict similar QSS vibrational energy distributions. This shows that the faster vibrational excitation for simulations using the NASA Ames PES (as seen in Sec. III B) facilitates the higher dissociation rates in simulations using the NASA Ames PES while maintaining similar depleted distributions in the QSS.
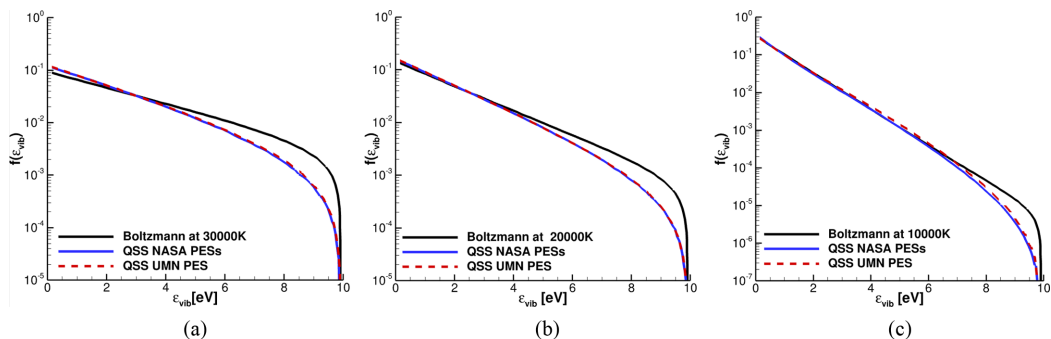
FIG. 7. Vibrational energy distribution of N_2 molecules in QSS for simulation including both $N_2 + N$ and $N_2 + N_2$ interactions, at (a) $T_t = 30\,000$ K, (b) $T_t = 20\,000$ K, and (c) $T_t = 10\,000$ K.

IV. HYPERSONIC DISSOCIATING NITROGEN FLOW PAST a CYLINDER

Recently, the DMS method has been expanded to perform 2D fluid flow simulations [41–43]. As the N_3 and N_4 PESs are designed to resolve high-energy collisions and are being used to develop thermochemical models for hypersonic flight [71,72], comparing the flow fields given by two independently developed sets of PESs provides a unique opportunity to compare thermochemical characteristics predicted by PESs in an applied fluid dynamics scenario. In this section we discuss results comparing a Mach 20 dissociating nitrogen flow over a cylinder predicted by the NASA PESs and the UMN PES. We have used this case in the past to compare thermochemical characteristics of the UMN PES [9,10] to an updated version [73] of the UMN PES where the single-point energy data base was expanded from 16 547 to 21 406 single-point energy points [42,73]. It was concluded that the original UMN PES [9,10] is sufficiently resolved and adding new single energy points for the data set did not meaningfully alter the solution [42]. While the new UMN PES compared in Ref. [42] was an improvement on the original and used the same quantum methods, the NASA PES provides a point of comparison outside the UMN data set and uses different quantum methods (discussed in Sec. II B).

A. Simulation setup

For the Mach 20 dissociating flow simulations the freestream density is set to $\rho_0 = 0.0184$ kg/m^3 and temperature $T = T_t = T_r = T_v = 226$ K, which corresponds to nominal conditions at 30 km with a freestream velocity $u = 6130$ m/s. The cylinder diameter $D_c = 0.2$ mm and the cylinder surface is assumed to be adiabatic, i.e., all particles colliding with the wall are specularly reflected and there is no thermal or inertial accommodation at the cylinder surface. The Knudsen number based on the freestream isKn ≈ 0.015, which is in the range where Navier-Stokes solution (CFD) should also be valid.

The grid is refined and coarsened in a manner the enforces the local grid size $\Delta x < 1.2\lambda_l$, where λ_l is the local mean-free path. A further refinement is done to the cells in the stagnation region such that $\Delta x < 0.6\lambda_l$ to provide high resolution of the bow shock. The DMS time step is $\Delta t_{\mathrm{DMS}} = 5 \times 10^{-11}$ s.

B. Thermochemistry in the flow field

Figure 8 shows the translational [Fig. 8(a)], rotational [Fig. 8(b)], and vibrational [Fig. 8(c)] temperatures and the mass fraction of atomic nitrogen [Fig. 8(d)] from the 2D DMS calculations of Mach 20 flow over the cylinder. The top half of the images shows the flow field obtained using the UMN PES [9,10] and the bottom half shows the flow field obtained by using the NASA PESs [11,12]. Figure 8(a) shows that the two PESs predict similar translational temperature fields
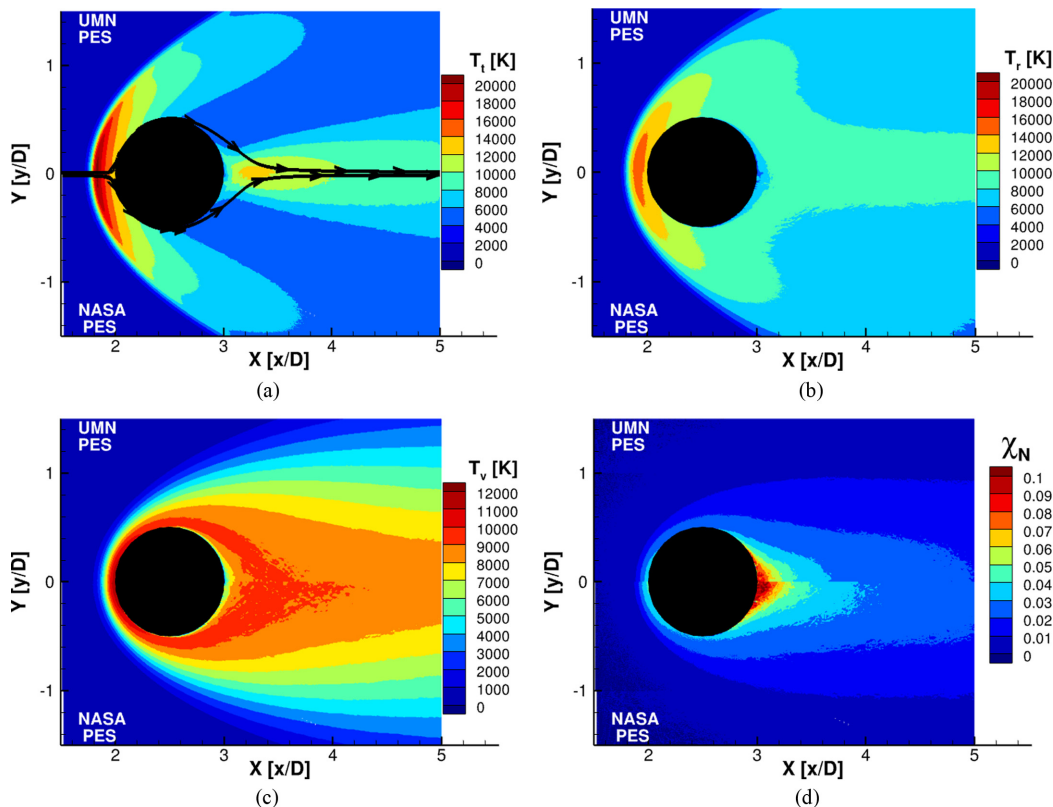
FIG. 8. Temperatures and composition of the Mach 20 flow field: (a) translational temperature, (b) rotational temperature, (c) vibrational temperature, and (d) mass fraction of atomic nitrogen..

and predict the same shock standoff distance. From Fig. 8(b) we can see that both simulations predict similar rotational temperature profiles, with the simulation using the NASA PESs rotationally deexciting slightly faster in the expansion region ($x/D > 2.5$). Figure 8(c) shows that the vibrational temperature field predicted by the two simulations is comparable in the compression region ($x/D < 2.5$) but the simulation using the NASA PESs is vibrationally hotter in the expansion region ($x/D > 2.5$).

Figure 8(d) shows that the mass fraction of atomic nitrogen in the simulation using the NASA PES is higher than for the simulation using the UMN PES. The results also show that most of the production of the atomic nitrogen occurs in the stagnation region; however, the cylinder wake has the highest mass fraction of the atomic nitrogen. Recall that no recombination reactions are included in these DMS calculations.

Figure 9(a) shows the variation of translational (blue), rotational (black), and vibrational (red) temperatures along the streamlines included in Fig. 8(a). It can be seen that all three energy modes are excited across the bow shock. The translational and rotational modes quickly equilibrate behind the shock, whereas the vibrational mode is only partially excited. As the flow travels over the cylinder and subsequently expands, there is a consistent drop in translational temperature while the rotational and vibrational modes freeze in a state of thermal nonequilibrium because the relaxation time for these modes is on the same order as the flow timescales. In the cylinder wake there is a peak in translational temperature associated with the closing of the streamlines behind the cylinder. However, the translation temperature relaxes towards thermal equilibrium as the flow accelerates
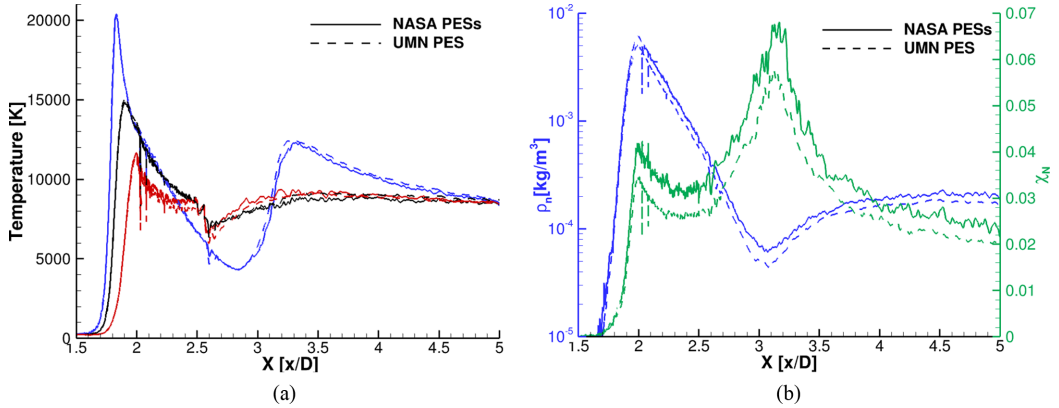
FIG. 9. Temperatures and composition along streamlines shown: (a) temperatures and (b) atomic nitrogen mass fraction and partial density.

behind the cylinder, while the rotational and vibrational modes continue to remain essentially frozen in this regime.

Figure 9(b) shows the partial density of atomic nitrogen (blue) and the mass fraction (green) along the same streamlines. It can be seen that both the partial density and mass fraction of atomic nitrogen increase behind the shock as molecular nitrogen dissociates in the compression region ($1.5 < x/D < 2$). Following the profile downstream within $2 < x/D < 3$, there is a drop in partial density that is attributed to the decrease in total density due to expansion. As the streamline closes around $x/D \sim 3.25$ the partial density starts increasing again. Meanwhile, the mass fraction of atomic nitrogen drops within $2 < x/D < 2.5$ due to volumetric expansion of the fluid. Within $2.5 < x/D < 3.5$ a peak in the mass fraction of atomic nitrogen is observed. This peak is attributed to the high translational temperatures in this region and the low fluid velocity that promotes dissociation in the rarefied region behind the cylinder. As the fluid expands further downstream we see a drop in mass fraction of atomic nitrogen due to continued flow expansion and relaxation back towards equilibrium.

C. Stagnation region

Figure 10(a) shows the temperatures and composition along the stagnation streamline. It can be seen that both simulations give the same shock standoff distance for the translational temperature. The translation and rotational modes excite and equilibrate behind the shock, whereas the vibrational mode only partially excites behind the shock. As can be seen at the wall ($x/D = 2$), the transrotational temperature for the simulation using the UMN PES is slightly higher than the simulation using the NASA PESs. This can be attributed to a lower level of dissociation in the UMN PES simulation. This difference in the degree of dissociation results in a stagnation point mass fraction of atomic nitrogen of 0.034 for the UMN PES simulation and 0.042 for the simulation that used the NASA PESs. This corresponds to a difference of over 23% in atomic mass fraction, which could have additional implications for nonspecular surfaces.

Figure 10(b) shows the vibrational energy distribution along the stagnation streamline at selected points $x/D = 1.8$ (dashed line), $x/D = 1.9$ (solid line), and $x/D = 2.0$ (dash-dotted line). It can be seen that the energy distribution functions predicted by the two simulations using different PESs are virtually identical at all three points. At $x/D = 1.8$ the population in the low vibrational levels is populated in a manner similar to a Boltzmann distribution corresponding to this temperature, but the mid- and high-energy levels are overpopulated when compared to the corresponding Boltzmann distribution, resulting in a highly non-Boltzmann distribution. At $x/D = 1.9$ we see a deviation from Boltzmann behavior at both low and high vibrational levels. At $x/D = 2.0$, vibrational energy
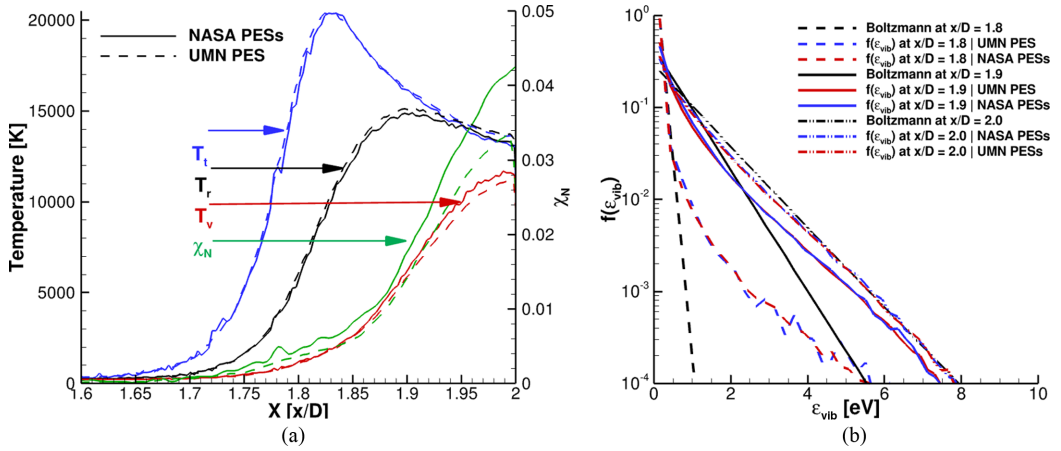
FIG. 10. (a) Temperature and composition and (b) vibrational distribution functions along stagnation streamline.

distributions still deviate slightly from Boltzmann behavior. This indicates that the vibrational excitation process, between the shock front ($x/D = 1.8$) and the stagnation point ($x/D = 2.0$), has a non-Boltzmann nature for this type of flow.

D. Cylinder flank

Figure 11(a) shows the temperature and composition profiles normal to the cylinder surface at the flank ($x/D = 2.5$). It can be seen that the translational temperature profile (blue) has two peaks. The first peak at $y/D = 1.2$ is due to the sampling line intersecting the oblique shock at $x/D = 2.5$. The second, broader peak around $y/D = 0.8$ is due to advection of shock heated gas from the stagnation region. At $y/D < 0.8$ a decrease in translational temperature is observed as the flow expands along the cylinder. Figure 11(a) also shows the rotational temperature (black) along this wall normal. It can be seen that the region is in rotational nonequilibrium, $T_r > T_t$ for $y/D < 1.0$. Here the rate of molecular interactions that equilibrate translational and rotational modes is slower
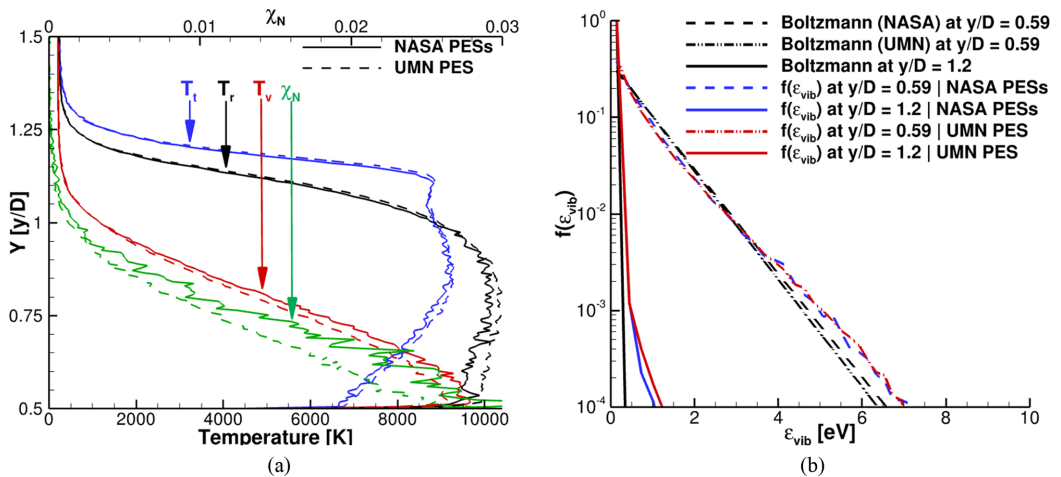

FIG. 11. (a) Temperature and composition and (b) vibrational distribution functions along the flank of the cylinder.
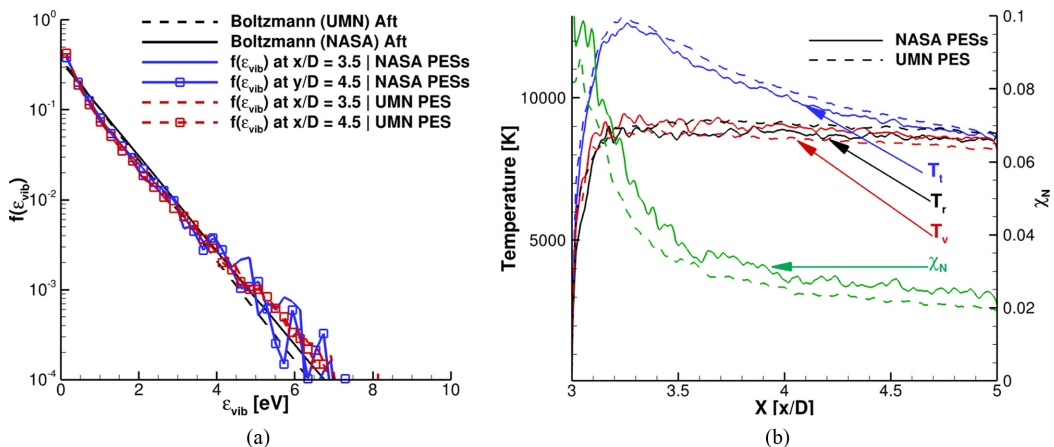
FIG. 12. (a) Temperature and composition and (b) vibrational distribution functions along the aft of the cylinder.

than the rate at which the translational temperature cools due to expansion of the flow. A similar trend is observed for the vibrational mode.

Additionally, the solutions obtained using the NASA PESs (solid line) and the UMN PES (dashed line) are qualitatively similar along this sampling profile. There are some quantitative differences starting at $y/D \approx 1$, where the rotational mode for the simulation using the UMN PES is hotter than the simulation using the NASA PESs. Conversely, in this region, the simulation using the NASA PES is vibrationally hotter. Interestingly, results yielded by the NASA PESs are in rotational-vibrational equilibrium near the cylinder surface. This is not seen with the UMN PES and shows that the simulations using the NASA PESs have faster internal energy relaxation. Additionally, the system has a higher mass fraction of atomic nitrogen for the simulation using the NASA PESs, which is consistent with the observations made in the sections above.

Figure 11(b) shows the vibrational energy distribution at $y/D = 0.59$ and 1.20. All data corresponding to statistics collected $y/D = 1.2$ are presented with a solid line. At $y/D = 1.2$ we notice that the vibrational energy distribution varies slightly from the corresponding Boltzmann distribution; however, this deviation is observed to be less severe than that observed for the vibrational energy distribution $x/D = 1.8$ in Fig. 10(b). This is because the weaker oblique shock at the flank leads to less energetic molecular collisions than the stronger normal shock and therefore causes less deviation from Boltzmann behavior.

Figure 11(b) includes two sets of Boltzmann distributions for $y/D = 0.59$ because $T_v = 9000$ K when using the NASA PESs, but only 8700 K in the UMN PES. The black dashed curve corresponds to the Boltzmann distribution for $T_v = 9000$ K and is to be compared with the blue dashed curve showing the vibrational energy distribution obtained from the simulation using the NASA PESs. The DMS predicted solution deviates slightly from the Boltzmann distribution and exhibits behavior similar to that seen in the near-wall distribution of $x/D = 2$ in Fig. 10(b). The black dash-dotted curve shows the Boltzmann distribution for $T_v = 8700$ K and is used as a comparison point for for the vibrational energy distribution function obtained from the simulation that uses the UMN PES. It can be seen that both simulations produce similar slightly non-Boltzmann behavior at this location in the flow.

E. Cylinder aft

Figure 12(a) shows the temperature and composition profiles in the cylinder wake along the cylinder aft centerline. We see that the translational temperature (blue) peaks behind the cylinder at about $x/D = 3.25$, which is where the streamlines close behind the cylinder. As the flow expands

behind the cylinder, the translational temperature decreases. The rotational and vibrational modes remain frozen in the cylinder aft. It can be seen that the translational temperature given by the NASA PESs (blue solid curve) is slightly cooler than the translational temperature given by the UMN PES (blue dashed curve). Additionally, the rotational (black) and vibrational (blue) temperatures are in equilibrium in the simulation using the NASA PESs (solid curves) behind the shock at $T_r = T_v \sim$ 9250 K, whereas the rotational and vibrational modes are frozen in a nonequilibrium state for the simulation using the UMN PES (dashed curves), with $T_r \sim 9500$ K and $T_v \sim 8700$ K. As such, the NASA PESs simulation results in a slightly higher mass fraction of atomic nitrogen.

Figure 12(b) shows the vibrational energy distributions given by the simulation using the NASA PESs (blue solid curves) and UMN PES (red dashed curves) at $x/D = 3.5$ (line) and 4.5 (line with symbols). Additionally, we provide Boltzmann distribution at $T_v = 9250$ K (black solid line) to compare the NASA PES simulation and at $T_v = 8700$ K (black dashed line) to compare the UMN PES simulations. The distributions for both simulations do not change between $x/D = 3.5$ and 4.5 and are qualitatively similar. Also, these distributions exhibit minor deviation from the corresponding Boltzmann distributions, akin to the non-Boltzmann behavior seen at $y/D = 0.59$ in Fig. 11(b) and $x/D = 2.0$ in Fig. 10(b).

V. CONCLUSION

In this article we have presented a comparative atomic level study analyzing the vibrational excitation and dissociation of molecular nitrogen due to $N_2(^1\Sigma_g^+) + N(^4S_u)$ and $N_2(^1\Sigma_g^+) + N_2(^1\Sigma_g^+)$ interactions governed by independently developed potential energy surfaces at the University of Minnesota [9,10] and NASA Ames Research Center [11,12] at temperatures relevant at hypersonic reentry conditions. Vibrational excitation was studied for $N_2 + N_2$ interactions from $T = 10\,000$ to $30\,000$ K and for $N_2 + N$ from $T = 5000$ to $30\,000$ K. A maximum variation of 16% was found for the predicted characteristic vibrational excitation time constant due to $N_2 + N_2$ interactions and 28% for $N_2 + N$ interactions, with the difference decreasing with an increase in temperature. Furthermore, nonequilibrium dissociation was studied from $T = 10\,000$ to $30\,000$ K under the quasi-steady-state conditions. It was observed that the two PESs give the same non-Boltzmann distributions in the QSS regime. However, the QSS dissociation rate coefficients were found to differ by 50% for both $N_2 + N_2$ and $N_2 + N$ interactions at $10\,000$ K. This difference decreases with an increase in temperature.

In addition, an inviscid Mach 20 dissociating nitrogen flow over a cylinder was studied with the DMS method using the two sets of independently developed PESs. This flow was characterized by rotational and vibrational excitation, dissociation, and thermal nonequilibrium throughout the flow field. The simulations using the NASA PESs and the UMN PES were shown to qualitatively predict similar flow features. However, it was observed that the NASA PES allows for slightly faster vibrational excitation and quicker vibrational-rotational equilibration in the flow field. The simulation using the NASA PES also predicted a higher fraction of atomic nitrogen in the flow field, with the maximum difference of atomic nitrogen mass fraction being about 28% in the cylinder wake.

It was observed that the vibrational energy distributions have a non-Boltzmann nature during the vibrational excitation in the stagnation region of the flow, with both simulations predicting similar deviation from Boltzmann behavior. Similarly, non-Boltzmann distributions were observed in the expanding flow along the flank and aft of the cylinder and both simulations provided a similar description of the non-Boltzmann characteristics of the flow field.

In conclusion, independently developed PESs at the University of Minnesota [9,10] and NASA Ames Research Center [11,12] for $N_2 + N_2$ and $N_2 + N$ interactions were used to simulate heat baths and a canonical dissociating hypersonic flow. In these simulations, these interactions on these PESs produced remarkably similar results for macroscopic and microscopic properties of the flow. Such favorable comparison yields confidence in the use of *ab initio* PESs to obtain thermochemical characteristics of reacting hypersonic flow.

ACKNOWLEDGMENTS

---

[1] G. V. Candler, Rate effects in hypersonic flows, Annu. Rev. Fluid Mech. **51**, 379 (2019).

[2] C. Park, Assessment of a two-temperature kinetic model for dissociating and weakly ionizing nitrogen, J. Thermophys. Heat Transfer **2**, 8 (1988).

[3] C. Park, Review of chemical-kinetic problems of future NASA missions, I: Earth entries, J. Thermophys. Heat Transf. **7**, 385 (1993).

[4] C. Park, J. T. Howe, R. L. Jaffe, and G. V. Candler, Review of chemical-kinetic problems of future NASA missions, II: Mars entries, J. Thermophys. Heat Transf. **8**, 9 (1994).

[5] S. Byron, Shock-tube measurement of the rate of dissociation of nitrogen, J. Chem. Phys. **44**, 1378 (1966).

[6] D. J. Kewley and H. G. Hornung, Free-piston shock-tube study of nitrogen dissociation, Chem. Phys. Lett. **25**, 531 (1974).

[7] J. P. Appleton, M. Steinberg, and D. J. Liquornik, Shock-tube study of nitrogen dissociation using vacuum-ultraviolet light absorption, J. Chem. Phys. **48**, 599 (1968).

[8] R. K. Hanson and D. Baganoff, Shock-tube study of nitrogen dissociation rates using pressure measurements, AIAA J. **10**, 211 (1972).

[9] Y. Paukku, K. R. Yang, Z. Varga, and D. G. Truhlar, Global *ab initio* ground-state potential energy surface of N_4, J. Chem. Phys. **139**, 044309 (2013).

[10] J. D. Bender, P. Valentini, I. Nompelis, Y. Paukku, Z. Varga, D. G. Truhlar, T. E. Schwartzentruber, and G. V. Candler, An improved potential energy surface and multi-temperature quasiclassical trajectory calculations of $N_2 + N_2$ dissociation reactions, J. Chem. Phys. **143**, 054304 (2015).

[11] G. Chaban, R. Jaffe, D. W. Schwenke, and W. Huo, *Proceedings of the 46th AIAA Aerospace Sciences Meeting and Exhibit, Reno, 2008* (AIAA, Reston, 2008), paper 1209.

[12] R. Jaffe, D. Schwenke, and G. Chaban, *Proceedings of the 10th AIAA/ASME Joint Thermophysics and Heat Transfer Conference, Chicago, 2010* (AIAA, Reston, 2010), Vol. 4517.

[13] Z. Varga, Y. Paukku, and D. G. Truhlar, Potential energy surfaces for $O + O_2$ collisions, J. Chem. Phys. **147**, 154312 (2017).

[14] Y. Paukku, K. R. Yang, Z. Varga, G. Song, J. D. Bender, and D. G. Truhlar, Potential energy surfaces of quintet and singlet O_4, J. Chem. Phys. **147**, 034301 (2017).

[15] Y. Paukku, Z. Varga, and D. G. Truhlar, Potential energy surface of triplet O_4, J. Chem. Phys. **148**, 124314 (2018).

[16] P. Valentini, M. S. Grover, and E. Josyula, Constructing feed-forward artificial neural networks to fit potential energy surfaces for molecular simulation of high-temperature gas flows, Phys. Rev. E **102**, 053302 (2020).

[17] Z. Varga, Y. Liu, J. Li, Y. Paukku, H. Guo, and D. G. Truhlar, Potential energy surfaces for high-energy $N + O_2$ collisions, J. Chem. Phys. **154**, 084304 (2021).

[18] D. G. Truhlar and J. T. Muckerman, *Atom-Molecule Collision Theory: A Guide for the Experimentalist* (Plenum, New York, 1979).

[19] G. D. Billing and E. Fisher, VV and VT rate coefficients in N_2 by a quantum-classical model, Chem. Phys. **43**, 395 (1979).

[20] A. Fernández-Ramos, J. A. Miller, S. J. Klippenstein, and D. G. Truhlar, Modeling the kinetics of bimolecular reactions, Chem. Rev. **106**, 4518 (2006).

[21] M. Capitelli, C. M. Ferreira, B. F. Gordiets, and A. I. Osipov, *Plasma Kinetics in Atmospheric Gases* (Springer Science + Business Media, New York, 2013), Vol. 31.

[22] G. Colonna, L. D. Pietanza, and M. Capitelli, Recombination-assisted nitrogen dissociation rates under nonequilibrium conditions, J. Thermophys. Heat Transfer **22**, 399 (2008).

[23] A. Munafò, A. Lani, A. Bultel, and M. Panesi, Modeling of non-equilibrium phenomena in expanding flows by means of a collisional-radiative model, Phys. Plasmas **20**, 073501 (2013).

[24] J. G. Kim and I. D. Boyd, Monte Carlo simulation of nitrogen dissociation based on state-resolved cross sections, Phys. Fluids **26**, 012006 (2014).

[25] E. Josyula and W. F. Bailey, Vibration-dissociation coupling using master equations in nonequilibrium hypersonic blunt-body flow, J. Thermophys. Heat Transfer **15**, 157 (2001).

[26] A. Sahai, B. Lopez, C. Johnston, and M. Panesi, Adaptive coarse graining method for energy transfer and dissociation kinetics of polyatomic species, J. Chem. Phys. **147**, 054107 (2017).

[27] R. Macdonald, R. Jaffe, D. Schwenke, and M. Panesi, Construction of a coarse-grain quasi-classical trajectory method. I. Theory and application to N_2-N_2 system, J. Chem. Phys. **148**, 054309 (2018).

[28] M. Panesi, R. L. Jaffe, D. W. Schwenke, and T. E. Magin, Rovibrational internal energy transfer and dissociation of $N_2(^1\Sigma_g^+) - N(^4S_u)$ system in hypersonic flows, J. Chem. Phys. **138**, 044312 (2013).

[29] D. A. Andrienko and I. D. Boyd, Rovibrational energy transfer and dissociation in O_2–O collisions, J. Chem. Phys. **144**, 104301 (2016).

[30] Y. Liu, M. Vinokur, M. Panesi, and T. Magin, *Proceedings of the 10th AIAA/ASME Joint Thermophysics and Heat Transfer Conference, Chicago, 2010* (Ref. [12]), paper No. 4332.

[31] M. Panesi and A. Lani, Collisional radiative coarse-grain model for ionization in air, Phys. Fluids **25**, 057101 (2013).

[32] E. V. Kustova and E. A. Nagnibeda, Kinetic model for multi-temperature flows of reacting carbon dioxide mixture, Chem. Phys. **398**, 111 (2012).

[33] R. Macdonald, M. Grover, T. Schwartzentruber, and M. Panesi, Construction of a coarse-grain quasi-classical trajectory method. I against the direct molecular simulation method, J. Chem. Phys. **148**, 054310 (2018).

[34] T. E. Schwartzentruber, M. S. Grover, and P. Valentini, Direct molecular simulation of nonequilibrium dilute gases, J. Thermophys. Heat Transf. **32**, 892 (2018).

[35] P. Valentini, T. E. Schwartzentruber, J. D. Bender, I. Nompelis, and G. V. Candler, Direct molecular simulation of nitrogen dissociation based on an *ab initio* potential energy surface, Phys. Fluids **27**, 086102 (2015).

[36] P. Valentini, T. E. Schwartzentruber, J. D. Bender, and G. V. Candler, Dynamics of nitrogen dissociation from direct molecular simulation, Phys. Rev. Fluids **1**, 043402 (2016).

[37] E. Torres and T. E. Schwartzentruber, *AIAA Scitech 2019 Forum* (AIAA, Reston, 2019), p. 1049.

[38] M. S. Grover, T. E. Schwartzentruber, Z. Varga, and D. G. Truhlar, *Proceedings of the 2018 AIAA Aerospace Sciences Meeting, Kissimmee, 2018* (AIAA, Reston, 2018), p. 0238.

[39] M. S. Grover, E. Torres, and T. E. Schwartzentruber, Direct molecular simulation of internal energy relaxation and dissociation in oxygen, Phys. Fluids **31**, 076107 (2019).

[40] E. Torres and T. E. Schwartzentruber, Direct molecular simulation of oxygen dissociation across normal shocks, Theor. Comput. Fluid Dyn. **36**, 41 (2022).

[41] M. S. Grover and P. Valentini, *Ab initio* simulation of hypersonic flows past a cylinder based on accurate potential energy surfaces, Phys. Fluids **33**, 051704 (2021).

[42] P. Valentini, M. S. Grover, N. Bisek, and A. Verhoff, Molecular simulation of flows in thermochemical non-equilibrium around a cylinder using *ab initio* potential energy surfaces for $N_2 + N$ and $N_2 + N_2$ interactions, Phys. Fluids **33**, 096108 (2021).

[43] M. S. Grover, P. Valentini, N. J. Bisek, and A. M. Verhoff, *AIAA SCITECH Forum, San Diego, 2022* (AIAA, Reston, 2022), p. 0873.

[44] P. Valentini, M. S. Grover, N. J. Bisek, and A. M. Verhoff, *AIAA SCITECH Forum, San Diego, 2022* (Ref. [43]), p. 0875.

[45] G. A. Bird, *Molecular Gas Dynamics and Simulation of Gas Flows* (Cambridge University Press, Cambridge, 1994).

[46] D. Frenkel and B. Smit, *Understanding Molecular Simulation: From Algorithms to Applications* (Academic, San Diego, 2002).

[47] E. C. Geistfeld, E. Torres, and T. E. Schwartzentruber, *AIAA SCITECH Forum, San Diego, 2022* (Ref. [43]), p. 1635.

[48] C. Kondur and K. A. Stephani, Rate constants and molecular recombination pathways of oxygen from quasi-classical trajectory simulations of the O_3 system, Chem. Phys. **552**, 111357 (2022).

[49] S. Plimpton, S. Moore, A. Borner, A. Stagg, T. Koehler, J. Torczynski, and M. Gallis, Direct simulation Monte Carlo on petaflop supercomputers and beyond, Phys. Fluids **31**, 086101 (2019).

[50] M. S. H. Ling and M. Rigby, Towards an intermolecular potential for nitrogen, Mol. Phys. **51**, 855 (1984).

[51] H. Eyring and M. Polanyi, Uber einfache gasreaktionen, Z. Phys. Chem. B **12**, 279 (1931).

[52] P. London, Probleme der modernen physik (Sommerfeld Festschrift), Z. Elektrochem. **35**, 552 (1929).

[53] S. Sato, On a new method of drawing the potential energy surface, J. Chem. Phys. **23**, 592 (1955).

[54] S. Sato, Potential energy surface of the system of three atoms, J. Chem. Phys. **23**, 2465 (1955).

[55] M. Karplus, R. N. Porter, and R. D. Sharma, Exchange reactions with activation energy. I. Simple barrier potential for (H, H_2), J. Chem. Phys. **43**, 3259 (1965).

[56] R. L. Jaffe, D. W. Schwenke, M. Grover, P. Valentini, T. E. Schwartzentruber, S. Venturi, and M. Panesi, *Proceedings of the 54th AIAA Aerospace Sciences Meeting, San Diego, 2016* (AIAA, Reston, 2016), p. 0503.

[57] T. H. Dunning, Jr., Gaussian basis sets for use in correlated molecular calculations. I. The atoms boron through neon and hydrogen, J. Chem. Phys. **90**, 1007 (1989).

[58] R. A. Kendall, Jr., T. H. Dunning, Jr, and R. J. Harrison, Electron affinities of the first-row atoms revisited. Systematic basis sets and wave functions, J. Chem. Phys. **96**, 6796 (1992).

[59] G. D. Purvis III and R. J. Bartlett, A full coupled-cluster singles and doubles model: The inclusion of disconnected triples, J. Chem. Phys. **76**, 1910 (1982).

[60] R. J. Gdanitz and R. Ahlrichs, The averaged coupled-pair functional (ACPF): A size-extensive modification of MR CI(SD), Chem. Phys. Lett. **143**, 413 (1988).

[61] B. O. Roos, P. R. Taylor, and P. E. M. Si, A complete active space SCF method (CASSCF) using a density matrix formulated super-CI approach, Chem. Phys. **48**, 157 (1980).

[62] R. J. Le Roy, Y. Huang, and C. Jary, An accurate analytic potential function for ground-state N_2 from a direct-potential-fit analysis of spectroscopic data, J. Chem. Phys. **125**, 164310 (2006).

[63] E. Papajak, H. R. Leverentz, J. Zheng, and D. G. Truhlar, Efficient Diffuse Basis Sets: cc-pVxZ+ and maug-cc-pVxZ, J. Chem. Theory Comput. **5**, 1197 (2009).

[64] K. Andersson, P. Malmqvist, and B. O. Roos, Second-order perturbation theory with a complete active space self-consistent field reference function, J. Chem. Phys. **96**, 1218 (1992).

[65] H. J. Werner, Third-order multireference perturbation theory The CASPT3 method, Mol. Phys. **89**, 645 (1996).

[66] J. Finley, P. Malmqvist, B. O. Roos, and L. Serrano-Andrés, The multi-state CASPT2 method, Chem. Phys. Lett. **288**, 299 (1998).

[67] R. L. Jaffe, *Proceedings of the 22nd Thermophysics Conference, Honolulu, 1987* (AIAA, Reston, 1987), p. 1633.

[68] M. S. Grover, Direct molecular simulation of nitrogen and oxygen at hypersonic conditions, Ph.D. thesis, University of Minnesota, 2018.

[69] R. C. Millikan and D. R. White, Systematics of vibrational relaxation, J. Chem. Phys. **39**, 3209 (1963).

[70] R. L. Macdonald, E. Torres, T. E. Schwartzentruber, and M. Panesi, State-to-state master equation and direct molecular simulation study of energy transfer and dissociation for the N_2–N system, J. Phys. Chem. A **124**, 6986 (2020).

[71] R. S. Chaudhry and G. V. Candler, *AIAA Scitech 2019 Forum* (Ref. [37]), p. 0789.

[72] N. Singh and T. Schwartzentruber, Consistent kinetic–continuum dissociation model I. Kinetic formulation, J. Chem. Phys. **152**, 224302 (2020).

[73] J. Li, Z. Varga, D. G. Truhlar, and H. Guo, Many-body permutationally invariant polynomial neural network potential energy surface for N_4, J. Chem. Theory Comput. **16**, 4822 (2020).